The DOI for this manuscript is doi: 10.1175/JCLI-D-17-0569.1

The final published version of this manuscript will replace the preliminary version at the above DOI once it is available.

If you would like to cite this EOR in a separate work, please use the following full citation:

Deng, K., S. Yang, M. Ting, Y. Tan, and S. He, 2018: Global Monsoon Precipitation: Trends, Leading Modes and Associated Drought and Heat Wave in the Northern Hemisphere. J. Climate. doi:10.1175/JCLI-D-17-0569.1, in press.

Global Monsoon Precipitation: Trends, Leading Modes and Associated Drought and Heat Wave in the Northern Hemisphere

Kaiqiang Deng[1], Song Yang[1-3]*, Mingfang Ting[4], Yaheng Tan[1] and Shan He[1]

[1] *School of Atmospheric Sciences, Sun Yat-sen University, Guangzhou, China*

[2] *State Key Laboratory of Severe Weather, Chinese Academy of Meteorological Science, Beijing, China*

[3] *Guangdong Province Key Laboratory for Climate Change and Natural Disaster Studies, Sun Yat-sen University, Guangzhou, China*

[4] *Lamont-Doherty Earth Observatory, Columbia University, Palisades, New York, USA*

Revised for *Journal of Climate*

April 2018

**Corresponding author address*: Prof. Song Yang, School of Atmospheric Sciences, Sun Yat-sen University, 135 West Xingang Road, Guangzhou 510275, China. E-mail: yangsong3@mail.sysu.edu.cn

ABSTRACT

Global monsoon precipitation (GMP) brings majority of water for the local agriculture and ecosystem. The Northern Hemisphere (NH) GMP shows an upward trend over the past decades, while the trend in the Southern Hemisphere (SH) GMP is weak and insignificant. The first three Singular Value Decomposition modes between NH GMP and global SST during boreal summer respectively reflect the Atlantic Multi-decadal Oscillation (AMO), Eastern Pacific (EP) ENSO, and Central Pacific (CP) ENSO, when the AMO dominates the NH climate and contributes to the increased trend. However, the first three modes between SH GMP and global SST during boreal winter are revealed as EP ENSO, the AMO, and CP ENSO, when EP ENSO becomes the most significant driver to the SH GMP and the AMO induced rainfall anomalies may cancel out with each other within the SH GM domain and thus result in a weak trend. The intensification of NH GMP is proposed to favor the occurrences of drought and heat wave (HW) in the middle latitudes through a monsoon–desert like mechanism. That is, the diabatic heating associated with the monsoonal rainfall may drive large–scale circulation anomalies and trigger intensified subsidence in remote regions. The anomalously descending motions over the middle latitudes are usually accompanied by clear skies, which result in less precipitation, more downward solar radiation, and thus drier and hotter soil conditions that favor the occurrences of droughts and HWs. In comparison, the SH GMP may exert much smaller impacts on the NH extremes in spring and summer, probably because the winter signals associated with SH GMP cannot sufficiently persist into the following seasons.

1. Introduction

The word “monsoon” comes from the Arabic word “mausam” and is referred to as a phenomenon of seasonal cycles of winds and rainfall (Ramage 1971). Compared to individual regional monsoons, the global monsoon (GM) emphasizes the integrated nature of global–scale reversal of atmospheric circulation and dry–wet alternation of rainfall (Trenberth et al. 2000; Qian et al. 2000). It is reported that there is more than 70% of the Earth’s population being affected by the GM precipitation (GMP) (Mohtadi et al. 2016), which produce majority of water for the local agriculture and ecosystem. The GMP also acts as a crucial source of latent heat, which drives global–scale atmospheric circulation and may influence the weather and climate outside the monsoon regions through atmospheric transportation of heat and momentum fluxes (Krishnan 2009; Vellore et al. 2015).

Great effort has been devoted to determining the trends of GMP in a warming world. Based on observations, the GMP is found to have significantly intensified in the recent decades, due mainly to an upward trend in the NH summer oceanic monsoon precipitation (Zhou et al., 2008; Hsu et al., 2011; Wang et al., 2012). In future warming scenarios, the Fifth Assessment Report of Intergovernmental Panel on Climate Change (IPCC–AR5) has reported that the GMP is likely to strengthen in the 21st century with remarkable increases in both area and intensity (Hsu et al., 2012, 2013; Kitoh et al., 2013). Moreover, the onset dates of GM are projected to advance and the retreat dates are projected to delay, resulting in lengthening of the GM season (Lee and Wang 2014). The enhancement of GMP has triggered increasing interest in climate community to investigate the physical causes of GMP variability.

The mechanisms behind the strengthening GMP could be complex due to the various drivers and all kinds of physical processes involved. Among the potential drivers, the increase in atmospheric moisture associated with the warming of atmosphere is believed to be the most effective one that causes an increase in total monsoon rainfall (e.g., Held and Soden 2006; Wentz et al. 2007; Richter and Xie 2008). Besides, the sea surface temperature anomalies (SSTAs) are also viewed as an important factor that may lead to the enhancement of GMP. For example, Liu et al. (2009) have attributed the increased NH GMP to the intensified temperature difference between the Northern and Southern Hemispheres, i.e., warmer SST in the NH than that in the SH. Wang et al. (2012) have suggested that the enhanced east–west thermal contrast in the Pacific Ocean also contributes to the strengthened GMP. In addition to the trends, the GMP shows close connections with dominant SST modes, such as El Niño – Southern Oscillation (ENSO) and the Atlantic Multi-decadal Oscillation (AMO). ENSO can significantly affect the Asian–Australian and West African monsoons through the Walker circulation, equatorial Rossby waves, and the Kelvin waves (e.g., Webster and Yang 1992; Wang et al. 2000; Joly and Voldoire 2009). The phase shift of AMO, from previous negative phases to post positive phases around mid–1990s, is also reported to increase the rainfall over the GM regions (Wang et al. 2013; Lopez et al. 2016; Kamae et al. 2017), implying that the GMP could be affected by not only greenhouse warming but also natural variability.

It is worth noting that both GMP and the leading modes of global SSTs present specific seasonally–dependent features. During the boreal summer, the GMP is located over the NH, when ENSO intensity is weakest and the AMO – related signals dominate the NH climate

(Semenov et al. 2010; Wyatt et al. 2012), suggesting a more intimate relationship between the NH GMP and the AMO. During the boreal winter, however, the GMP shifts into the SH, when ENSO becomes a primary driver to the SH climate (Karoly 1989; Garreaud and Battisti 1999) as the AMO signals are confined to the NH, suggesting a more robust relationship between the SH GMP and ENSO. However, a comprehensive examination to the relationship between GMP and the dominant SST modes from a seasonally–dependent perspective is still lacked, which will be one of the main goals of this study.

In addition, although there have been numerous studies investigating the GMP trends and their attributions, the impacts of GMP on the NH weather and climate, such as droughts and heat waves (HWs), have received less attention. Huang et al. (2016) have indicated that the mid-latitude dry land has expanded substantially in the past decades, corresponding to more intense, more frequent, and longer lasting heat waves (HWs) (Meehl and Tebaldi 2004). Wang et al. (2012) have proposed that the enhanced GMP not only amplifies the annual cycle of tropical climate but also promotes directly a “wet-gets-wetter” trend pattern and indirectly a “dry-gets-drier” trend pattern through a “monsoon–desert” – like mechanism. That is, the diabatic heating in monsoon region can induce a subsidence in the remote area and promote the occurrence of severe droughts (Rodwell and Hoskins 1996). Trenberth and Fasullo (2012) and Trenberth et al. (2015) have discussed the 2010 Russian summer HW and other climate extremes and concluded that the unusually abundant atmospheric moisture for nearby monsoons, owing to abnormal high SSTAs, could alter the atmospheric circulation that has a direct link to the higher latitudes, which may affect the middle-latitude extremes. Therefore, there is also a need to assess the impact of GMP on the NH extremes.

The current study will revisit the relationship between GMP and the global SST from a seasonally–dependent perspective, i.e., during the boreal summer (NH GMP) and winter (SH GMP), attempting to understand the roles of seasonal cycle in affecting the dominant modes between GMP and the global SST. Furthermore, we will also discuss the variation of GMP and explore its impacts on weather and climate in the NH, focusing on the drought and HW. The remainder of this paper is organized as follows. In section 2, we describe the data and method used in this study. In section 3, we discuss the seasonal changes and trends in GMP. The dominant modes between GMP and the global SST are documented in section 4. Relationships between NH/SH GMP and the NH extremes are addressed in section 5, followed by a summary in section 6.

2 Data and Method

a. Observation and model output

We apply two data sets of precipitation to depict the GMP for the purpose of comparison. They are the Global Precipitation Climatology Project (GPCP; Adler et al. 2003) and the Climate Prediction Center (CPC) Merged Analysis of Precipitation (CMAP; Xie and Arkin 1997), with a resolution of 2.5°×2.5° for the period of 1979 – present. Yin et al. (2004) have compared the precipitation products of GPCP and CMAP, and indicated that the CMAP is higher than the GPCP in tropical oceans, but the feature is reversed in the high-latitude oceans. They have emphasized that the use of atoll data by the CMAP is disputable, and the decreasing trend in the CMAP oceanic precipitation may be an artifact of input data change and atoll sampling error. In general, oceanic precipitation represented by the GPCP is more reasonable. In Fig. 2, we show the GMPs calculated from both GPCP and CMAP data sets to examine the trends and compare their differences. In other figures, the relationship between GMP and the other variables are evaluated based on the GPCP data set due to its better representation of tropical oceanic rainfall.

The monthly Extended Reconstructed Sea Surface Temperature Version 4 (ERSSTv4; Huang et al. 2015) and the Interpolated Outgoing Longwave Radiation (OLR; Liebmann and Smith 1996) data sets are available from the NOAA/OAR/ESRL PSD, Boulder, Colorado, USA (at the website: *http://www.esrl.noaa.gov/psd/*), with horizontal resolutions of 2°×2° and 2.5°×2.5° for the periods of 1854–present and 1974–2014, respectively. In comparison with previous versions, the SST in ERSSTv4 can better represent the El Niño/La Niña behavior. One problem in using the OLR data is that missing grids and missing values with grids are often present, presumably owing to satellite problems, archival problems, or incomplete global coverage. In the interpolated version, the missing values have been removed by temporal and spatial interpolation (Liebmann 1996). The OLR is often used as a surrogate for upper-level divergence (Chelliah et al. 1988). In the tropics, it is impossible to derive the divergence directly because of the dearth of upper-air stations, so one must rely on an assimilation model. Comparisons of divergence fields from various meteorological centers have shown large differences between different estimates (Trenberth and Olson 1988; Sardeshmukh and Liebmann 1993); thus, OLR is often deemed a more reliable indicator of tropical divergence than that derived from global wind analyses.

The other observational data sets are available from the European Centre for Medium-range Weather Forecasts (ECMWF) ERA-Interim (Dee et al. 2011), including the monthly geopotential height, three-dimensional velocities at multiple levels and the 4-layer volumetric soil moisture, with a resolution of 2.5°×2.5° for the period of 1979 – present, which are used to diagnose the large-scale features associated with the GMP. The ERA-Interim reanalysis data set has removed the inhomogeneities apparent in the earlier ERA-40 data set by employing improved data assimilation techniques (Dee et al. 2011). Simmons et al. (2010) have reported that the newer reanalysis data set is significantly better than the ERA-40 at replicating monthly variability in surface temperature. Moreover, Cornes and Jones (2013) have shown that the ERA-Interim reanalysis data sets are generally very good at replicating both the seasonally and spatially varying trends in extreme surface temperature. Thus, we select this data set to analyze extreme HWs.

Zhang et al. (2017) have compared the abilities of three atmospheric general circulation models (AGCMs), each with two resolution configurations, in reproducing the GMP, and shown that model resolutions may affect the simulation of GMP. Therefore, this study applies five AGCMs, with different horizontal resolutions, to assess the impact of ENSO/AMO on the GMP. These model outputs are from the AGCM experiments forced by observed SST for the period of 1979-2015, using ECHAM5, CFSv2, CAM4, GEOS5, and CCM3 models. The horizontal resolutions of the models are 0.75°×0.75°, 1°×1°, 1.25°×0.75°, 1.25°×1°, and 2.5°×2.5°, respectively. These 5 AGCM experiments are carried out by the NOAA Drought Task Force (DTF) (Schubert et al., 2009), which are available from the Lamont-Doherty

Earth Observatory. We adopt these DTF simulations because they have relatively good skills in reproducing the NH drought/heat. These AGCM experiments are conducted between 12 to 20 ensemble members depending on the model. We have calculated the ensemble means for each model before analyzing the results in this study.

b. Determinations of GM domain, droughts and HWs

There are various metrics to define a GM domain, such as the divergence in the upper troposphere (Trenberth et al. 2000), the annual precipitation range (Wang and Ding 2006), and the k-means clustering method and low-level cross-equatorial flow (Jiang et al. 2016), among which the approach proposed by Wang and Ding (2006, 2008) has been used most widely due to its relative simplicity. Wang and Ding (2008) have demonstrated that the GM can be represented by two major modes of the annual variation, namely, a solstitial mode (71%) and an equinoctial asymmetric mode (13%), which peak respectively in JJAS/DJFM and April–May (AM)/October–November (ON). In this study, we will analyze the so-called solstitial mode of GM, namely the JJAS/DJFM monsoons (Lin et al. 2014; Yan et al. 2016). The GM domain is identified based on Wang and Ding (2008): (1) the annual range of precipitation between wet and dry seasons exceeds 3 mm/day and (2) the wet seasonal (e.g., JJAS in the NH) precipitation contributes more than 50% of the total annual precipitation. Using this method, the GM domain can be separated into six sectors (see Fig. 1a).

The Dai PDSI is applied to assess the severity of drought (Dai et al. 2004; Dai 2011a, 2011b). The PDSI has renewed several versions, such as the self-calibrating PDSI (sc_PDSI) and the PDSI using improved formulations for potential evapotranspiration (PE), such as the

Penman-Monteith equation (pm_PDSI) instead of the Thornthwaite equation (th_PDSI). Dai (2011) has compared and evaluated the original PDSI and revised PDSI indices, and indicated that the choice of the PE only has small effects on both the PDSI and the sc_PDSI for the 20th century climate. All four forms of the PDSI show similar correlations with observed monthly soil moisture in North America and Eurasia, and present consistent drying trends in mid-latitude regions. In this study, we use the Dai PDSI, which can be acquired from the NOAA/OAR/ESRL PSD website. According to the degrees of severity, droughts are further classified into moderate, severe, and extreme types, when seasonal mean PDSI meets the following conditions: $-3<\mathrm{PDSI}\leqslant-2$, $-4<\mathrm{PDSI}\leqslant-3$, and $\mathrm{PDSI}\leqslant-4$, respectively (e.g., Alley 1984, 1985; Wells et al. 2004).

The HW threshold is computed based on a 95th percentile method for the daily maximum 2m temperature (Mx2t) (e.g., Meehl and Tebaldi 2004; Della-Marta et al. 2007; Kuglitsch et al. 2010). For a specific day within the summer season (June-September), the Mx2t threshold is identified by the 95th percentile of Mx2t for a total of 37 years multiplied by 15 days (the 15 days represent the seven days on either side of the target date) for the period from 1979 to 2015. By moving the 15-day sample windows forward and backward, we are able to obtain consecutive thresholds for every day. Therefore, we can obtain the HW days (HWD) by computing the total days of Mx2t exceeding the 95th-precentile threshold, which reflects the HW frequency and duration in each summer (Wu et al. 2012). The categories of moderate, severe, and extreme HWs are determined by the conditions of $5<\mathrm{HWD}\leqslant10$, $10<\mathrm{HWD}\leqslant15$, and $\mathrm{HWD}>15$, respectively. It should be noted that the selections of HWD thresholds 5, 10, and 15 are empirical, but further examinations indicate that the slight changes of HWD thresholds would not change the conclusion in this study.

The Singular Value Decomposition (SVD) analysis is used to explore the covariability between GMP and global SST, which allows us to identify their concurrent modes (Bretherton et al. 1992; Wallace et al. 1992). In fact, Trenberth et al. (2002) have made a systematic investigation to the covariability of SST and the divergence of atmospheric energy transport, using the SVD analysis of the temporal covariance, and revealed that ENSO is dominant in the first two modes, explaining 62% and 12% of the covariance in the Pacific domain and explaining 39.5% and 15.4% globally for the first and second modes, respectively. In this study, we decompose the covariability between GMP and global SST from a seasonally-dependent perspective, i.e. during the boreal summer and winter, given that the GMP is featured by strong seasonal cycles. It should be noted that only the precipitation within the GM domains is considered in our SVD analysis. After that, we compute the correlation between the global precipitation and the time series of precipitation for the leading SVD modes to better analyze the physical connections between GMP and global SSTAs. The trends in GMP are calculated by the method of linear regression. The statistical significance in correlation analysis is assessed using the Student's *t*-test with a degree of freedom of 35 for a total of 37 years (1979–2015).

3. Seasonal changes and trends in GMP

Figure 1 shows the domains of GM and associated atmospheric circulation patterns. The GM domains can be generally separated into six sectors (Fig. 1a), including West Africa

(WAF), Asia–northwestern Pacific (ANWP), and North America (NAM) in the NH; and East Africa (EAF), Australia (AUS), and South America (SAM) in the SH. All of these sub-monsoons locate over the land – sea transitional regions, where the strongest thermal contrast between continent and ocean exists.

Figures 1(b) and 1(c) show the upper-tropospheric divergent wind and OLR associated with the NH GMP and SH GMP, respectively. During the boreal summer (JJAS), strong upper-tropospheric divergent winds appear over the WAF, ANWP, and NAM regions, accompanied by vigorous convection. The NH subtropical divergent winds stretch toward the northern and southern hemispheres, and tend to converge over the Mediterranean Sea, the Eurasian continent, and the southern oceans. During the boreal winter (DJFM), the upper-tropospheric divergent wind and associated convection shift to the SH, concentrated over the EAF, AUS, and SAM regions, and tend to converge in the northern subtropics. Compared with the SH GM, the NH GM seems to be much stronger in terms of dry–wet alternation, divergent circulation, and convection.

Figures 2(a) and 2(b) present the linear trends in NH GMP and SH GMP, respectively, obtained from both GPCP and CMAP data sets. In general, the NH and SH GMPs calculated from the CMAP data set are prominently higher than those calculated from the GPCP data set. As mentioned in section 2, Yin et al. (2004) have already noted that the oceanic precipitation in the CMAP is higher than that in the GPCP. The GPCP product is believed to be more reasonable, as the use of atoll data by the CMAP is disputable. The year-to-year variability in GPCP GMP is highly correlated with the CMAP GMP, with a correlation coefficient of 0.76

(0.83) in the NH (SH). Both the GPCP and the CMAP NH GMPs show significant upward trends during the period of 1979–2015; however, the linear trends in the SH GMPs, obtained from the GPCP and the CMAP, are insignificant and seem to be contrary with each other.

As indicated by the Clausius-Clapeyron relation, the warming atmosphere is able to hold more water moisture and thus may bring more rainfall (Wentz et al. 2007). However, if the increased trend in NH GMP is driven by the warming atmosphere, why is the trend in SH GMP insignificant? One speculation is that, the asymmetric warmings between the two hemispheres, i.e., the NH atmosphere warms faster than the SH atmosphere (Kang et al. 2015), lead to a strengthened NH – SH temperature gradient that boosts the NH GMP and suppresses the SH GMP (Liu et al. 2012; Lee and Wang 2014). Nevertheless, other explanations, such as the oceanic forcing and multidecadal modulations associated with the Pacific/Atlantic dominant modes, are also possible, which will be discussed as follows.

4. Dominant modes between GMP and SST from seasonally-dependent perspective

The GMP migrates from the NH during the boreal summer to the SH during the boreal winter, which may be related with global SST. To assess the impacts of seasonal cycle on GMP – global SST relationship, a SVD analysis is applied to decompose the covariability between GMP and global SST, separately during the simultaneous summer (JJAS) and the simultaneous winter (DJFM). The spatial patterns of precipitation and SST for each mode are acquired by correlating them with the corresponding time series.

a. NH GMP and SST during boreal summer

During the boreal summer, the first SVD mode between the NH GMP and global SST accounts for 39.9% of the total covariance, reflecting the low-frequency effect from the Atlantic Multi-decadal Oscillation (AMO). As seen from Fig. 3(a), associated with the first mode, significantly warming SSTAs occur in the Atlantic, India, and the western Pacific Oceans. Correspondingly, increased precipitation is found over the NH GM domains. Figure 3(b) shows the PC1s and the unsmoothed AMO index, where the correlation coefficient between PC1 (SST) and the year-to-year AMO is 0.82, which suggests that the recent increased trend in the NH GMP be largely contributed by the AMO. Indeed, the AMO has experienced a dramatic phase shift around the mid-1990s, from previous negative to post positive phases, which induces widely warming in the Atlantic and Indo-Pacific regions. The warming SSTAs may promote more water moisture being evaporated into the atmosphere and thus increase the rainfall over the NH GM domains.

The second mode explains about 25.4% of the total covariance, revealing a feature of Eastern Pacific (EP) ENSO. As shown in Fig. 3(c), significant warmings appear in the central–eastern Pacific and the Indian Ocean, accompanied by a moderate cooling in the western Pacific. Correlated with EP warming, suppressed rainfall appears over the Maritime Continent–North Australia, Central America, West Africa, and vice versa. Figure 3(d) shows the PC2s and NINO3 index, where the correlation coefficient between PC2 (SST) and the EP ENSO (NINO3) is 0.85, implying that the EP ENSO is an important driver to modulate the interannual variability of the NH GMP.

The third mode explains 9.6% of the total covariance, which seems to be associated with the Central Pacific (CP) ENSO (Ashok et al. 2007). As indicated by Fig. 3(e), the third mode is characterized by a significant cooling in the central Pacific and warming in the southeastern Pacific, which is corresponding to increased rainfall over the eastern Pacific and Central America and decreased rainfall over the WAF and ANWP regions. It should be noted that, although the SST pattern shows cooling in the CP region during boreal summer, it is actually evolved from the antecedent winter El Niño that shows warming SSTA in the CP. Figure 3(f) shows the PC3s and the preceding winter NINO4 index, where the correlation coefficient between PC3 (SST) and the preceding CP ENSO (NINO4, DJFM) is 0.44, exceeding the 99% confidence level, suggesting that the CP ENSO also plays a role in affecting the year-to-year variations of NH GMP.

b. SH GMP and SST during boreal winter

During the boreal winter, the GMP peaks over the SH. As seen from Fig. 4, the first, second, and third SVD modes between SH GMP and global SST respectively explain 57.2%, 15.6%, and 4.8% of the total covariance, accounting for approximately 78% covariance in total, compared with 75% during the boreal summer. The first three modes during the boreal winter are basically unchanged compared with those during the boreal summer, but the orders between the first and the second modes exchange with each other, suggesting that the EP ENSO be the most significant driver to affect the SH GMP during the boreal winter.

As shown in Fig. 4(a), the EP warming is reflected in the first mode of SST, significantly correlated with decreased rainfall over South Africa, the Maritime Continent–Australia, and South America. Figure 4(b) show the PC1s and the NINO3 index, where the correlation coefficient between PC1 (SST) and the EP ENSO (NINO3) is 0.94. The second mode now reflects the AMO signal (Fig. 4c), which is significantly correlated with increased rainfall over South Africa and Australia, but decreased rainfall over South America, which may cancel out with each other and result in an insignificant trend in the total SH GMP. The correlation coefficient between PC2 (SST) and the unsmoothed AMO is 0.82 (Fig. 4d). The third mode indicates the CP ENSO, which is similar to that during the boreal summer except for explaining a reduced percentage of the total covariance. As shown in Fig. 4(e), the precipitation anomalies induced by the CP ENSO is less coherent compared to those induced by the EP ENSO. In general, the CP warming tends to increase the oceanic rainfall, while suppress the land rainfall over the SH. Figure 4(f) depicts the PC3s and the NINO4 index, where the correlation coefficient between PC3 (SST) and the CP ENSO (NINO4) during the boreal winter is 0.31. As seen from Fig. 4(f), the NINO4 seems to match well with the PC3s series especially after the mid-1990s, probably due to the increasing intensity as well as occurrence frequency of the CP ENSO since the 1990s (Lee and McPhaden 2010).

c. AGCM simulations

Figures 5 and 6 illustrate the regression patterns of observed and simulated global precipitations onto the AMO/NINO3 index, during the boreal summer and winter, respectively. In general, all AGCMs have reproduced similar regression patterns shown in the observations regardless of the different resolutions for each AGCM.

During the boreal summer (Fig. 5), the strengthened AMO was simulated to increase precipitation over West Africa and Central America, and to decrease precipitation over ANWP. As seen from the right panel of Fig. 5, the EP warming was simulated to increase precipitation over the central–eastern Pacific, and to reduce precipitation over the whole NH GM regions. The AGCMs seemed to show a relatively poor skill in reproducing the precipitation pattern over AWNP. Compared with the observations, the AGCMs-simulated rainfall over Central America (ANWP) is overstated (understated).

During the boreal winter (Fig. 6), the intensified AMO was simulated to increase precipitation over Australia (same as the observations) and South America (contrary to the observations). As indicated by the right panels, the EP warming was simulated to suppress precipitation over the entire SH GM region that was consistent with the observations. In general, the AGCMs could better reproduce ENSO related precipitation pattern over the SH GM region, compared to that induced by the AMO. It should be noted that the CP warming was also simulated to decrease the NH/SH GMP (figure not shown), although the precipitation anomalies were smaller than those induced by the EP SSTA.

Briefly, during the boreal summer, the NH GMP is primarily influenced by the AMO, which boosts the increasing trend in NH GMP by a multidecadal modulation. During the boreal winter, however, the EP ENSO is the most significant driver to the interannual variability of the SH GMP, when the AMO – induced rainfall anomalies within the SH GM domains may cancel out with each other and thus result in an insignificant trend in the total SH GMP. The order changes between the first two SVD modes of GMP and global SST during different seasons are understandable given their annual cycle features. During the boreal summer, the GMP peaks over the NH, when ENSO is the weakest and the AMO – forced signals dominate the NH climate; during the boreal winter, the GMP shifts into the SH, when ENSO is the strongest and the AMO – related signals are mainly confined to the NH. Thus the NH GMP is primarily modulated by the AMO during the boreal summer, while the SH GMP is dominated by the EP ENSO during the boreal winter.

5. Impacts of GMP on NH drought and HW

a. Large-scale conditions associated with GMP

Figure 7(a) shows the anomalous atmospheric circulations associated with the NH GMP during the boreal summer. The intensification of NH GMP is significantly correlated with enhanced convection over West and Central Africa, South Asia, the northwestern Pacific, and Central America, and suppressed convection over South Africa, West Australia, and South America. In particular, anomalous divergent winds are induced in the subtropical upper troposphere, which stretch poleward and lead to suppressed convection over the entire NH middle latitudes. The anomalous strengthened convection and divergent winds over the WAF, ANWP, and NAM regions are coinciding with the suppressed convection and convergent winds over the NH middle latitudes, implying an intensified meridional circulation.

Figure 7(b) shows the anomalous atmospheric circulations associated with the SH GMP during the boreal winter. The intensification of SH GMP is associated with enhanced convection over South Africa, the Maritime Continent – Australia and South America, accompanied by intensified upper tropospheric divergent winds over these regions. The emanated divergent winds converge over the Southern Indian and Pacific Oceans and the NH subtropical regions, leading to suppressed convection over the Middle East, East Asia, and the southern United States. No matter for the NH GMP or for the SH GMP, the correlated divergent winds in the upper troposphere are found to converge over the central and eastern Pacific, suggesting that the GMPs be closely tied to ENSO, as discussed in section 4.

Figure 8 shows the regression patterns of seasonal mean soil moisture and maximum 2m temperature (Mx2t) onto the normalized NH GMP index during the boreal summer, where the linear trends have been removed from the NH GMP. As seen from Fig. 8(a), drier soil conditions are observed in vast areas, including the Mediterranean Sea, Central Eurasia, and North America. Correspondingly, anomalous warmings appear in wide regions, especially the preferred areas including North America, West Russia, Central-East Asia, and the Mediterranean Sea, where the local convection is significantly suppressed due to the forced descending motions associated with the intensification of NH GMP.

It should be emphasized that the significant warmings over the Eurasian and North American continents may strengthen the thermal contrast between land and oceans, which could reinforce the NH GMP. In turn, the enhanced NH GMP would further intensify the descending branch of the forced meridional overturning circulation, resulting in anomalously suppressed convection and sinking motion in the NH middle latitudes. Such large–scale teleconnection between rising and sinking air masses is similar to the "warm land–cold ocean" mechanism of Wang et al. (2012) or the "monsoon–desert" mechanism of Cherchi et al. (2016), which indicates that the diabatic heating associated with the monsoonal rainfall could drive large–scale circulation anomalies and trigger abnormal subsidence in remote regions. The anomalous descending motions over the NH mid-latitude regions are usually accompanied by clear skies, which may result in less precipitation and more downward solar radiation, and thus drier and hotter soil conditions that favor the occurrence of droughts and HWs in the NH middle latitudes.

Figure 9 is similar to Fig. 8, but depicts the regression patterns of spring soil moisture (MAM) and summer Mx2t (JJAS) onto the antecedent winter SH GMP. The soil moisture is believed to have a seasonal–scale memory, which may help the SH GMP signals to persist into the following seasons. During the boreal spring, in response to an intensified SH GMP, drier soil moisture is observed in the NH subtropics, including North Africa, Middle East and the south United States (Fig. 9a). However, the SH GMP seems to show less significant impacts on the following summer temperature (Fig. 9b), suggesting that the NH summer HWs be irrelevant to the antecedent SH GMP. The failed linkage of SH GMP to the following summer surface temperature in the NH subtropics could be associated with the rapid growth of convective noises over monsoon regions and decay of ENSO amplitudes in the transitional season, which could obscure the previous SH GMP signals (Webster and Yang 1992).

b. Relationship between GMP and NH extremes

Figure 10 illustrates the scatter plots between NH GMP and NH mid-latitude droughts and between negative NINO3 index (i.e., La Niña) and NH mid-latitude droughts during the boreal summer, in order to compare the differences between NH GMP and ENSO in affecting the NH extremes. The area index of mid-latitude droughts (or HWs) in each year can be acquired by computing the number of grid points over land (30°N – 60°N), where the PDSI (or HWD for HWs) meets the criteria mentioned in section 2. A larger area index implies a broader domain where the extremes emerge.

As shown in the left panels of Fig. 10, an intensified NH GMP tends to be correlated with more widespread droughts. The correlation coefficients between the moderate, severe, extreme droughts and the NH GMP are 0.26, 0.37, and 0.36, respectively. Compared to the moderate droughts, the severe and extreme droughts show more close connection with the NH GMP. The right panels of Fig. 9 show the scatter plots of the moderate, severe, extreme droughts with ENSO (represented by negative NINO3 index), showing correlation coefficients of 0.14, 0.29, and 0.27, respectively, indicating that a cooling eastern Pacific may amplify the drought domain in the NH middle latitudes. In comparison, the correlation coefficients between drought and ENSO are much smaller compared with the correlation coefficients between drought and NH GMP. That is to say, ENSO alone cannot fully explain the significant relationships between mid-latitude drought and NH GMP. Indeed, ENSO is at its weakest phase during the boreal summer, and the other factors, such as the AMO, may greatly strengthen the NH GMP – mid-latitude drought relations.

Figure 11 shows the similar scatter plots between moderate, severe, extreme HWs and the NH GMP during the boreal summer, whose correlation coefficients are 0.18, 0.4, and 0.48, respectively. In general, the relationships of NH GMP with the HWs are more robust than that with the droughts. The increased occurrence of mid-latitude HWs likely results from the lower precipitation–lower evaporation feedback. That is, the precipitation deficits could lead to a drier soil and reduce the evaporation cooling, which in turn decrease the local precipitation, eventually resulting in severer droughts and increased hot weather events. The right panels of Fig. 11 indicate the relationships between moderate, severe, extreme HWs and

ENSO, whose correlation coefficients are -0.12, 0.26, and 0.37, respectively. Similarly, although the ESNO shows significant linkage to the mid-latitude HWs, the correlation coefficients are much weaker than that with the NH GMP, further demonstrating that ENSO is not the only factor that affects the NH GMP – NH extreme relationship.

Figure 12 (13) illustrate the relationships between spring drought (summer HWs) in the NH subtropics (10°N – 30°N) and the antecedent winter SH GMP. Unlike the NH GMP, the SH GMP seems to show weak relationships with the subtropical extremes (both droughts and HWs). As seen from Fig. 12, the intensified SH GMP is significantly correlated with a moderate drought in the following spring, with a correlation coefficient of 0.33. However, the correlations of SH GMP with severe and extreme droughts are insignificant. In comparison, the La Niña seems to favor the occurrence of subtropical droughts, although the correlation coefficients are also insignificant. As shown in Fig. 13, both the SH GMP and ENSO show insignificant correlation with the following summer HWs. The signals forced by the SH GMP or ENSO in the antecedent winter seem to fail to persist sufficiently into the following summer, which is consistent with the results shown in Fig. 9(b).

Finally, although the NH and SH GMPs may directly affect the NH climate through the modulation of meridional circulations, it should be cautious that the current study has not excluded the possible impact of SSTAs via planetary wave propagation. It is certain that both the GMP and the NH climate are affected by ENSO, and thus there must be some connections among them. However, this study has also pointed out that ENSO alone is insufficient to explain the significant relations between GMP and the NH climate and extremes. As revealed by the SVD analysis, the AMO and ENSO are the primary oceanic drivers to the GMP, and they dominate the GMP during the boreal summer and winter, respectively. Even if the impact of ENSO on the NH climate is realized via planetary waves, in most cases, tropical wave trains are found to originate from specific regions where strong latent heating exists. Such latent heating can be released by the GM rainfall.

6. Summary

The GM domain can be separated into 6 sectors, i.e., West Africa, Asia –Northwestern Pacific, North America in the NH during boreal summer, and East Africa, Australia, South America in the SH during boreal winter. The NH GMP shows an increasing trend for the period of 1979 – 2015, while the trend in SH GMP is insignificant. The strengthened NH GMP may result from the greenhouse warming and the multi-decadal modulation of AMO.

During the boreal summer, the first three SVD modes between NH GMP and global SST reflect the AMO, the EP ENSO and the CP ENSO, respectively. Associated with the AMO, significant warmings appear in the Atlantic, India, and the western Pacific Oceans, which may lead to more water moisture being evaporated into the atmosphere that increases the NH GMP. The EP and CP warmings are generally associated with suppressed rainfall over the NH GM domains, and vice versa. During the boreal summer, the GMP locates over the NH, when ENSO intensity is weakest and the AMO could dominate the NH climate. The phase shift of AMO, from previous negative to the post positive phases, is proposed to contribute to the upward trend in the NH GMP.

During the boreal winter, the first three SVD modes between SH GMP and global SST respectively indicate the EP ENSO, the AMO, and the CP ENSO, where the orders of the first two modes change with each other. The EP warming tends to suppress the rainfall over the entire SH GM domain. However, the AMO is associated with increased rainfall over South Africa and Australia, and decreased rainfall over South America, which may cancel out with each other and thus result in an insignificant trend in the SH GMP.

The enhancement of NH GMP corresponds to stronger convection and intensified upper tropospheric divergent winds over the NH GM regions, which stretch poleward and trigger suppressed convection over the middle latitudes. As a result, less precipitation and drier soil appear over the vast areas of Eurasia and North America, which favor the occurrences of mid-latitude droughts and HWs. The connections between NH GMP and the mid-latitude droughts and HWs could be maintained and reinforced by a "monsoon–desert" like mechanism, which denotes that the diabatic heating associated with the monsoonal rainfall could trigger anomalous subsidence over remote regions by forcing large–scale atmospheric circulation. In comparison, the SH GMP shows much small impacts on the NH extremes. Although the enhancement of SH GMP tends to reduce the rainfall over NH subtropical regions and lead to a moderate drought during the boreal spring, its relationships with the severer spring droughts or the following summer HWs are insignificant. The SH GMP signals fail to persist into the following summers, as discussed in many previous studies, which could be related to the rapid growth of monsoon–related noise and the decay of ENSO amplitude during the transitional season.

Our study points at the importance of NH GMP to the NH mid-latitude droughts/HWs.

The seasonal cycles in GMP and ENSO determine that the AMO could be the most important oceanic driver that modulates the upward “trend” in NH GMP during the boreal summer. There are numerous studies that have investigated the impacts of Atlantic SSTAs on the droughts/HWs in North America and Eurasia by a mechanism of planetary wave propagation (e.g., McCabe et al. 2004; Qian et al. 2014; Zhou and Wu 2016). This study adds that the AMO and ENSO may also affect the NH extremes through a modulation of meridional atmospheric circulations that are driven by the intensification of NH GMP.

Acknowledgments. This study was supported by the National Key Scientific Research Plan of China (Grant 2014CB953904), the National Key Research and Development Program of China (2016YFA0602703), the National Natural Science Foundation of China (Grants 41690123, 41690120, 91637208, and 41661144019), LASW State Key Laboratory Special Fund (2013LASW－A05 and 2016LASW-B01), the “111-Plan” Project of China (Grant B17049), and the China Meteorological Administration Guangzhou Joint Research Center for Atmospheric Sciences.

REFERENCES

Adler, R.F., G.J. Huffman, and Coauthors, 2003: The Version 2 Global Precipitation Climatology Project (GPCP) Monthly Precipitation Analysis (1979-Present). *J. Hydrometeor.*, **4,** 1147-1167.

Ashok, K., S. K. Behera, S. A. Rao, H. Weng, and T. Yamagata, 2007: El Niño Modoki and its possible teleconnection. *J. Geophys. Res.*, **112,** C11007. doi:10.1029/2006JC003798.

Bretherton, C. S., C. Smith, and J. M. Wallace, 1992: An intercomparison of methods for finding coupled patterns in climate data. *J. Climate,* **5,** 541–560.

Chelliah, M., and P. Arkin, 1992: Large-scale interannual variability of monthly outgoing longwave radiation anomalies over the global Tropics. *J. Climate*, **5,** 371–389.

Cherchi, A., H. Annamalai, S. Masina, A. Navarra, and A. Alessandri, 2016: Twenty-first century projected summer mean climate in the Mediterranean interpreted through the monsoon-desert mechanism. *Climate Dyn.*, **47,** 2361–2371.

Collins, M., and Coauthors, 2010: The impact of global warming on the tropical Pacific and El Niño. *Nat. Geosci.*, **3,** 391–397, doi:10.1038/ngeo868.

Cornes, R. C., and P. D. Jones, 2013: How well does the ERA-Interim reanalysis replicate trends in extremes of surface temperature across Europe? *J. Geophys. Res.*, **118,** 10262–10276.

Dai, A., K. E. Trenberth, and T. Qian, 2004: A global data set of Palmer Drought Severity Index for 1870-2002: Relationship with soil moisture and effects of surface warming. *J.*

Hydrometeorology, **5,** 1117-1130.

Dai, A., 2010a: Drought under global warming: A review. *Wiley Interdiscip. Rev.: Climate Change*, **2,** 45–65, doi:10.1002/wcc.81.

Dai, A., 2011b: Characteristics and trends in various forms of the Palmer Drought Severity Index during 1900–2008. *J. Geophys. Res.*, **116,** D12115, doi:10.1029/2010JD015541.

Dee, D., and Coauthors, 2011: The ERA-Interim reanalysis: Configuration and performance of the data assimilation system. *Quart. J. Roy. Meteor. Soc.*, **137,** 553–597.

Della-Marta, P. M., J. Luterbacher, and Coauthors, 2006: Summer heat waves over western Europe 1880–2003, their relationship to large scale forcings and predictability. *Climate Dyn.*, **29,** 251–275.

Held, I. M., and B. J. Soden, 2006: Robust responses of the hydrological cycle to global warming. *J. Climate*, **19,** 5686–5699.

Hsu, P., T. Li, and B. Wang, 2011: Trends in global monsoon area and precipitation over the past 30 years. *Geophys. Res. Lett.*, **38,** L08701, doi:10.1029/2011GL046893.

Hsu, P., T. Li, J.-J. Luo, H. Murakami, A. Kitoh, and M. Zhao, 2012: Increase of global monsoon area and precipitation under global warming: A robust signal? *Geophys. Res. Lett.*, **39,** L06701, doi:10.1029/2012GL051037.

Hsu, P., T. Li, H. Murakami, and A. Kitoh, 2013: Future change of the global monsoon revealed from 19 CMIP5 models. *J. Geophys. Res.*, **18,** 1247–1260。

Huang B., V. F. Banzon, and co-authors 2015: Extended Reconstructed Sea Surface Temperature version 4 (ERSST.v4). Part I: Upgrades and intercomparison. *J. Climate*, **28,** 911–930.

Huang, J., H. Yu, X. Guan, G. Wang, and R. Guo, 2016b: Accelerated dryland expansion under climate change. *Nat. Climate Change*, **6,** 166–171.

Jiang, N., W. Qian, and J. H. Leung, 2016: The global monsoon division combining the k-means clustering method and low-level cross-equatorial flow. *Climate Dyn.*, **47,** 2345.

Joly, M., and A. Voldoire, 2009: Influence of ENSO on the West African monsoon: Temporal aspects and atmospheric processes. *J. Climate*, **22,** 3193–3210.

Kamae, Y., X. Li, S. Xie, and H. Ueda, 2017: Atlantic effects on recent decadal trends in global monsoon. *Climate Dyn.*, doi:10.1007/s00382-017-3522-3.

Kang, S. M., and Coauthors, 2015: Croll revisited: Why is the northern hemisphere warmer than the southern hemisphere? *Climate Dyn.*, **44,** 1457–1472.

Kitoh, A., H. Endo, K. Krishna Kumar, I. F. A. Cavalcanti, P. Goswami, and T. Zhou, 2013: Monsoons in a changing world: a regional perspective in a global context. *J. Geophys. Res.*, **118,** 3053–3065, doi:10.1002/jgrd.50258.

Krishnan, R., C. Zhang, and M. Sugi, 2000: Dynamics of breaks in the Indian summer monsoon. *J. Atmos. Sci.*, **57,** 1354–1372.

Kuglitsch, F. G., A. Toreti, and Coauthors, 2010: Heat wave changes in the eastern Mediterranean since 1960. *Geophys. Res. Lett.*, **37,** L04802.

Lau, W. K. M., and K.-M. Kim, 2012: The 2010 Pakistan flood and Russian heat wave: Teleconnection of hydrometeorological extremes. *J. Hydrometeor.*, **13,** 392–403.

Lee, J.-Y., and B. Wang, 2014: Future change of global monsoon in the CMIP5. *Climate Dyn.*,

42, 101–119.

Lee, T., and M. J. McPhaden, 2010: Increasing intensity of El Niño in the central-equatorial Pacific. *Geophys. Res. Lett.*, **37,** L14603, doi:10.1029/2010GL044007.

Liebmann B. and C. A. Smith, 1996: Description of a complete (interpolated) outgoing longwave radiation dataset. *Bull. Amer. Meteor. Soc.*, **77,** 1275-1277.

Liu, J., B. Wang, Q. Ding, X. Kuang, W. Soon and E. Zorita, 2009: Centennial variations of the global monsoon precipitation in the last millennium: results from ECHO-G model. *J. Climate*, **22,** 2356–2371.

Lopez, H., S. Dong, and S.-K. Lee, 2016: Decadal modulations of interhemispheric global atmospheric circulations and monsoons by the South Atlantic meridional overturning circulation. *Geophys. Res. Lett.*, **43,** 8250–8258.

McCabe, G. J., and M. A. Palecki, 2006: Multidecadal climate variability of global lands and oceans. *Int. J. Climatol.*, **26,** 849–865.

Meehl, G. A., and C. Tebaldi, 2004: More intense, more frequent and longer lasting heat waves in the 21st century. *Science*, **305,** 994–997.

Mohtadi, M., M. Prange, and S. Steinke, 2016: Palaeoclimatic insights into forcing and response of monsoon rainfall. *Nature*, **533,** 191–199.

Qian, C., J.-Y. Yu, and G. Chen, 2014: Decadal summer drought frequency in China: The increasing influence of the Atlantic Multi-decadal Oscillation. *Environ. Res. Lett.*, **9,** 124004, doi:10.1088/1748-9326/9/12/124004.

Qian W, 2000: Dry/wet alternation and global monsoon. *Geophys. Res. Lett.*, **27,** 3679–3682.

Ramage, C. S., 1971: *Monsoon Meteorology*. *International Geophysical Series*, **Vol. 15,** Academic Press, 296 pp.

Richter, I., and S-P. Xie, 2008: The muted precipitation increase in global warming simulations: A surface evaporation perspective. *J. Geophys. Res.*, **113,** D24118.

Rodwell, M. J., and B. J. Hoskins, 1996: Monsoons and the dynamics of deserts. *Quart. J. Roy. Meteor. Soc.*, **122,** 1385–1404.

Sardeshmukh, P. D., and B. Liebmann, 1993: An assessment of low-frequency variability in the Tropics as indicated by some proxies of tropical convection. *J. Climate*, **6,** 569–575.

Schubert, S., D. Gutzler, and Coauthors, 2009: A US CLIVAR Project to Assess and Compare the Responses of Global Climate Models to Drought-Related SST Forcing Patterns: Overview and Results. *J. Climate*, **22,** 5251–5272.

Semenov, V. A., M. Latif, D. Dommenget, N. S. Keenlyside, A. Strehz, T. Martin, and W. Park, 2010: The impact of North Atlantic – Arctic multidecadal variability on Northern Hemisphere surface air temperature. *J. Climate*, **23,** 5668–5677.

Simmons, A., K. M. Willett, P. D. Jones, P. W. Thorne, and D. P. Dee, 2010: Low-frequency variations in surface atmospheric humidity, temperature, and precipitation: Inferences from reanalyses and monthly gridded observational data sets. *J. Geophys. Res.*, **115,** D01110, doi:10.1029/2009JD012442.

Trenberth, and J. G. Olson, 1988: An evaluation and intercomparison of global analyses from NMC and ECMWF. *Bull. Amer. Meteor. Soc.*, **69,** 1047–1057.

——, D. P. Stepaniak, and J. M. Caron, 2000: The global monsoon as seen through the divergent atmospheric circulation. *J. Climate*, **13,** 3969–3993.

——, D. P. Stepaniak, and J. M. Caron 2002: Interannual variations in the atmospheric heat budget. *J. Geophys. Res.*, **107,** D8, 10.1029/2000JD000297.

——, and J. Fasullo, 2012: Climate extremes and climate change: The Russian heat wave and other climate extremes of 2010. *J. Geophys. Res.*, **117,** D17103.

——, J. Fasullo, and T. Shepherd, 2015: Attribution of climate extreme events. *Nat. Clim. Change*, **5,** 725–730.

Vellore, R., M. Kaplan, and co-authors, 2015: Monsoon-extratropical circulation interactions in Himalayan extreme rainfall. *Climate Dyn.*, **46,** 3517–3546.

Wang, B., R. Wu, and X. Fu, 2000: Pacific–East Asian teleconnection: How does ENSO affect East Asian climate? *J. Climate*, **13,** 1517–1536.

——, and Q. Ding, 2006: Changes in global monsoon precipitation over the past 56 years. *Geophys. Res. Lett.*, **33,** L06711, doi:10.1029/2005GL025347.

——, and Q. Ding, 2008: Global monsoon: Dominant mode of annual variation in the tropics. *Dyn. Atmos. Oceans*, **44,** 165–183.

——, J. Liu, H. Kim, P. Webster, and S. Yim, 2012: Recent change of the global monsoon precipitation (1979–2008). *Climate Dyn.*, **39,** 1123–1135.

——, J. Liu, H.-J. Kim, P. J. Webster, S.-Y. Yim, and B. Xiang, 2013: Northern Hemisphere summer monsoon intensified by mega-El Niño/Southern Oscillation and Atlantic multidecadal oscillation. *Proc. Natl. Acad. Sci. USA*, **110,** 5347–5352.

Webster, P. J., and S. Yang, 1992: Monsoon and ENSO: Selectively interactive systems. *Quart.*

J. Roy. Meteor. Soc.,**118,** 877–926

Wentz, F. J., L. Ricciardulli, K. Hilburn, and C. Mears, 2007: How much more rain will global warming bring? *Science*, **317,** 233–235.

Wu, Z., Z. Jiang, J. Li, S. Zhong, and L. Wang, 2012: Possible association of the western Tibetan Plateau snow cover with the decadal to interdecadal variations of Northern China heatwave frequency. *Climate Dyn.*, **39,** 2393–2402.

Wyatt, M., S. Kravtsov, and A. A. Tsonis, 2012: Atlantic Multidecadal Oscillation and Northern Hemisphere’s climate variability. *Climate Dyn.*, **38,** 929–949.

Xie, P., and P. A. Arkin, 1997: Global precipitation: A 17-year monthly analysis based on gauge observations, satellite estimates, and numerical model outputs. *Bull. Amer. Meteor. Soc.*, **78,** 2539 - 2558.

Yin, X. G., A. Gruber, and P. Arkin, 2004: Comparison of the GPCP and CMAP merged gauge-satellite monthly precipitation products for the period 1979-2001. *J. Hydrometeor.*, **5,** 1207–1222.

Zhang L., P. Wu, T. Zhou, M. Roberts, R. Schiemann, 2016: Added value of high resolution models in simulating global precipitation characteristics. *Atmos. Sci. Lett.*, **17,** 646-657.

Zhou, T., R. Yu, H. Li, and B. Wang, 2008: Ocean forcing to changes in global monsoon precipitation over the recent half-century. *J. Climate,* **21,** 3833–3852.

Zhou, Y., and Z. Wu, 2016: Possible impacts of mega-El Niño/Southern oscillation and Atlantic multidecadal oscillation on Eurasian heat wave frequency variability. *Quart. J. Roy. Meteor. Soc.*, **142,** 1647–1661.

List of Figure Captions

Figure 1. (a) GPCP seasonal precipitation differences between wet and dry seasons (JJAS minus DJFM for the Northern Hemisphere, and DJFM minus JJAS for the Southern Hemisphere), in which the global monsoon (GM) domains are outlined by red lines. (b) and (c) show maps of 200-hPa divergent wind (vector) and OLR (shading) during the boreal summer (JJAS) and winter (DJFM), respectively.

Figure 2. (a) Northern Hemisphere (NH) global monsoon precipitation (GMP) computed from area average over the WAF, ANWP, and NAM domains. The blue and green lines indicate the GPCP and CMAP data sets, respectively. (b) is the same as (a), but for the Southern Hemisphere (SH) GMP computed from area average over the EAF, AUS, and SAM domains. The linear trends in GMP are indicated by black/grey lines. The correlation coefficients (CORR) between GPCP and CMAP GMPs are plotted in the lower right corner.

Figure 3. Singular Value Decomposition (SVD) analysis between JJAS NH GMP and JJAS SST for the period of 1979–2015, where the heterogeneous correlation coefficient (CC) patterns and corresponding time series for each mode are shown in the left and right panels, respectively. The CC between PC1s/PC2s/PC3s for NH GMP and SST is 0.87/0.92/0.87. The CC between PC1/PC2/PC3 for the SST pattern and the JJAS unsmoothed year-to-year Atlantic Multi-decadal Oscillation (AMO)/JJAS NINO3/preceding DJFM NINO4 index is 0.82/0.85/0.44. The explained covariance is given in the parenthesis.

Figure 4. Same as Fig. 3, except for DJFM SH GMP and DJFM SST. The CC between

PC1s/PC2s/PC3s for SH GMP and SST is 0.92/0.90/0.89. The CC between PC1/PC2/PC3 for the SST pattern and the DJFM NINO3/DJFM unsmoothed year-to-year AMO/ DJFM NINO4 index is 0.94/0.82/0.31.

Figure 5. Regression maps of simulated JJAS global precipitation (unit: mm/day) onto the JJAS AMO (left) and NINO3 (right) indices. The AGCMs with different horizontal resolutions are indicated above each subplot.

Figure 6. Same as Fig. 5, except for the simulated DJFM global precipitation (unit: mm/day) regressed onto the DJFM AMO (left) and NINO3 (right) indices.

Figure 7. Correlation coefficients of OLR (shading) and 200-hPa divergent wind (vector) with the NH (a) and SH (b) GMP indices obtained from the GPCP data. The magnitudes of vectors indicate the square root of correlation coefficients of zonal and meridional velocities with PCs. The linear trends have been removed from the GMP indices.

Figure 8. (a) Regression of 0–200 cm soil moisture content (shading) (a) and maximum 2m temperature (Mx2t) (shading) (b) with the GPCP NH GMP index for boreal summer. The dotted areas indicate that the anomalies exceed the 90% confidence levels. The linear trends have been removed from the NH GMP index.

Figure 9. (a) Regression of 0–200 cm soil moisture content (shading) (a) and Mx2t (shading) (b) with the GPCP SH GMP. The soil moisture is for boreal spring, while the Mx2t is for boreal summer (JJAS). The dotted areas indicate that the anomalies exceed the 90% confidence levels. The linear trends have been removed from the SH GMP index.

Figure 10. Diagrams of normalized area indices of boreal summer droughts in mid-latitude

regions (30°N – 60°N) with respect to the concurrent GPCP NH GMP (left, JJAS)/negative NINO3.4 (right, JJAS), where the linear trends in NH GMP have been removed. The severity of drought is defined in section 2. The calculation of drought area indices are seen in the text. The correlation coefficients (CORR) are plotted in each panel.

Figure 11. Same as Fig. 10, except for the heat waves (HWs).

Figure 12. Same as Fig. 10, except for the boreal spring (MAM) droughts in subtropics (10°N – 30°N) with respect to the antecedent GPCP SH GMP (left, DJFM)/negative NINO3 (right, DJFM), where the linear trends in SH GMP have been removed.

Figure 13. Same as Fig. 10, except for the boreal summer (JJAS) HWs in subtropics (10°N – 30°N) with respect to the antecedent GPCP SH GMP (left, DJFM)/antecedent negative NINO3 (right, DJFM), where the linear trends in SH GMP have been removed.

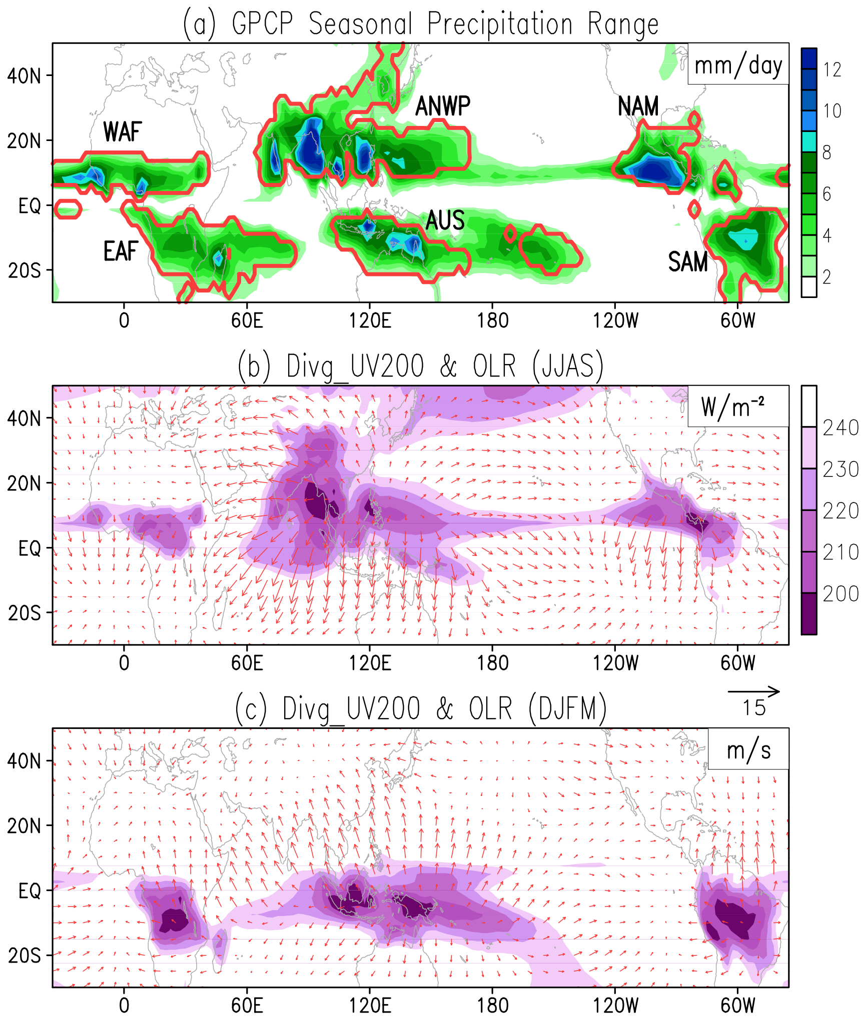

Figure 1. (a) GPCP seasonal precipitation differences between wet and dry seasons (JJAS minus DJFM for the Northern Hemisphere, and DJFM minus JJAS for the Southern Hemisphere), in which the global monsoon (GM) domains are outlined by red lines. (b) and (c) show maps of 200-hPa divergent wind (vector) and OLR (shading) during the boreal summer (JJAS) and winter (DJFM), respectively.

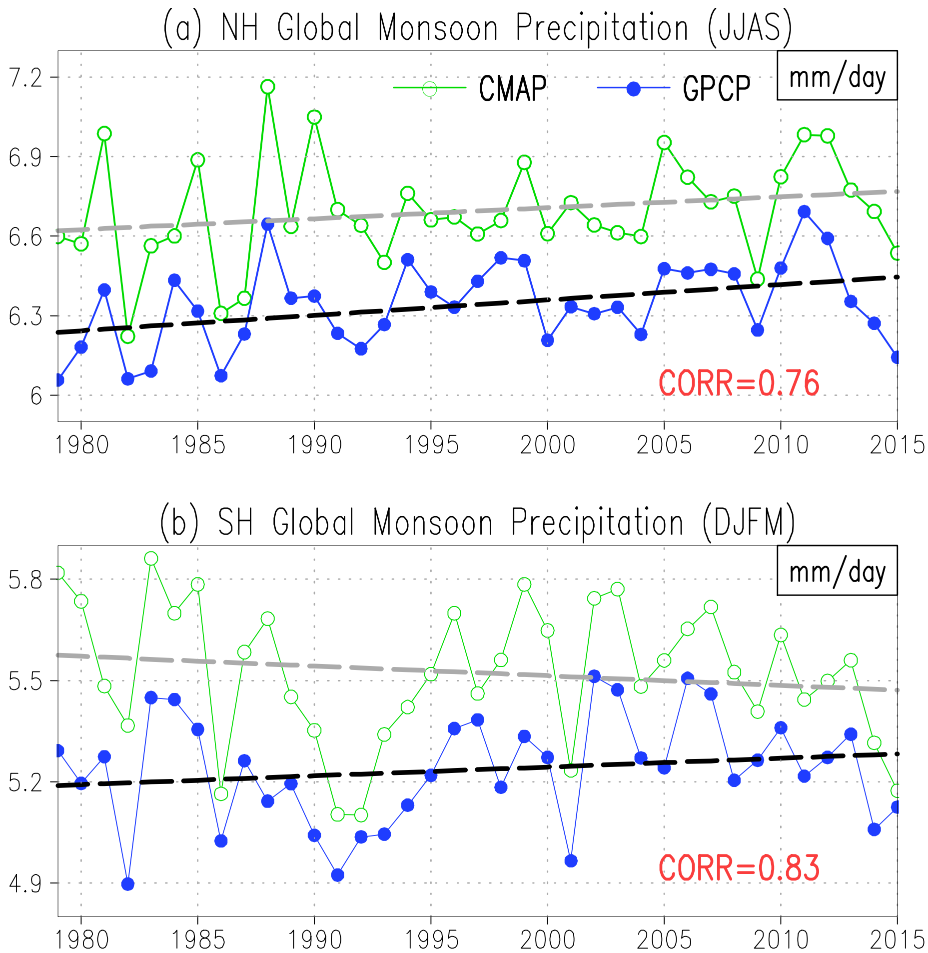

Figure 2. (a) Northern Hemisphere (NH) global monsoon precipitation (GMP) computed from area average over the WAF, ANWP, and NAM domains. The blue and green lines indicate the GPCP and CMAP data sets, respectively. (b) is the same as (a), but for the Southern Hemisphere (SH) GMP computed from area average over the EAF, AUS, and SAM domains. The linear trends in GMP are indicated by black/grey lines. The correlation coefficients (CORR) between GPCP and CMAP GMPs are plotted in the lower right corner.

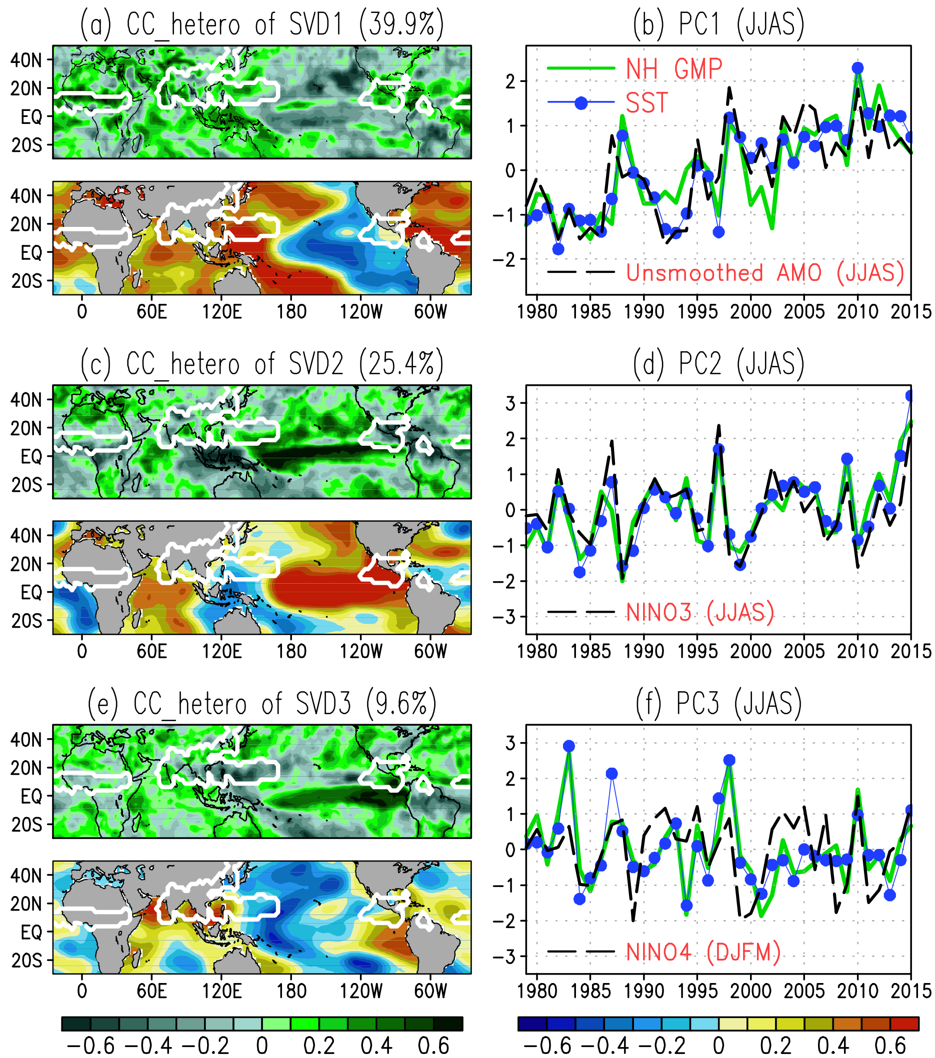

Figure 3. Singular Value Decomposition (SVD) analysis between JJAS NH GMP and JJAS SST for the period of 1979–2015, where the heterogeneous correlation coefficient (CC) patterns and corresponding time series for each mode are shown in the left and right panels, respectively. The CC between PC1s/PC2s/PC3s for NH GMP and SST is 0.87/0.92/0.87. The CC between PC1/PC2/PC3 for the SST pattern and the JJAS unsmoothed year-to-year Atlantic Multi-decadal Oscillation (AMO)/JJAS NINO3/preceding DJFM NINO4 index is 0.82/0.85/0.44. The explained covariance is given in the parenthesis.

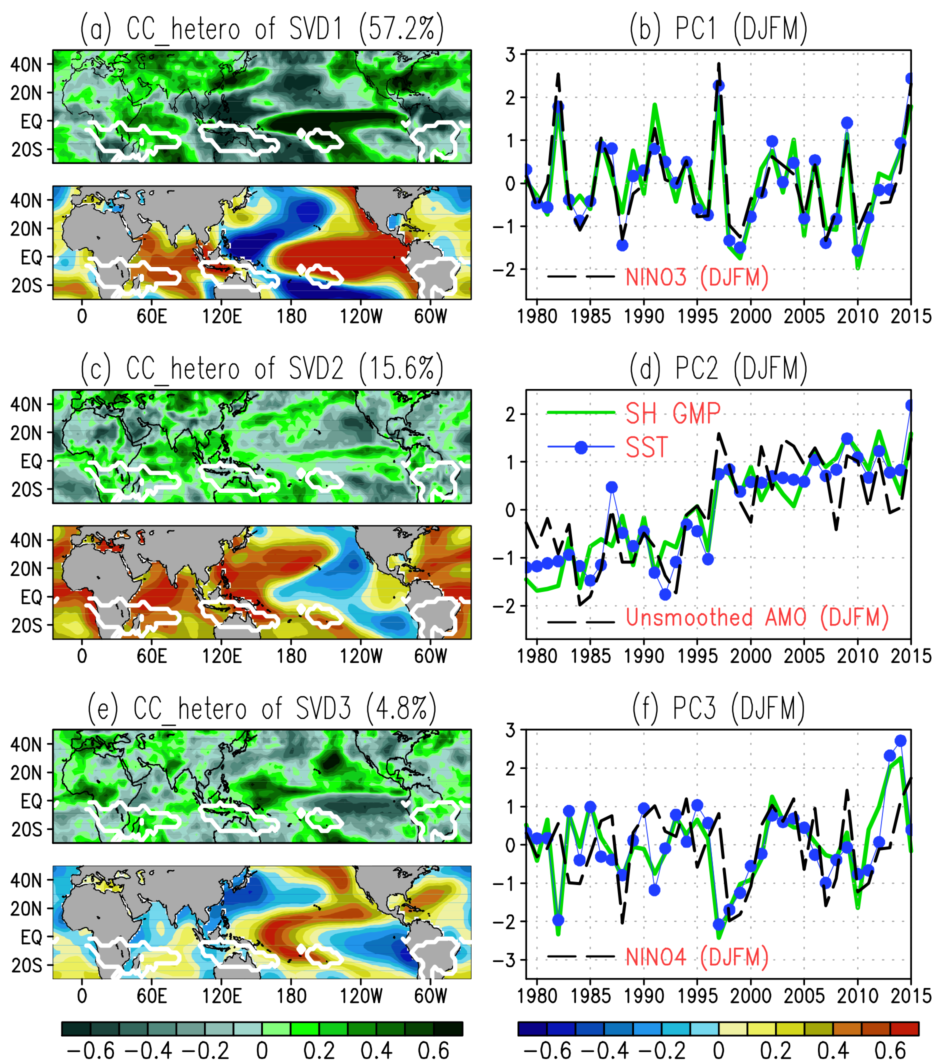

Figure 4. Same as Fig. 3, except for DJFM SH GMP and DJFM SST. The CC between PC1s/PC2s/PC3s for SH GMP and SST is 0.92/0.90/0.89. The CC between PC1/PC2/PC3 for the SST pattern and the DJFM NINO3/DJFM unsmoothed year-to-year AMO/ DJFM NINO4 index is 0.94/0.82/0.31.

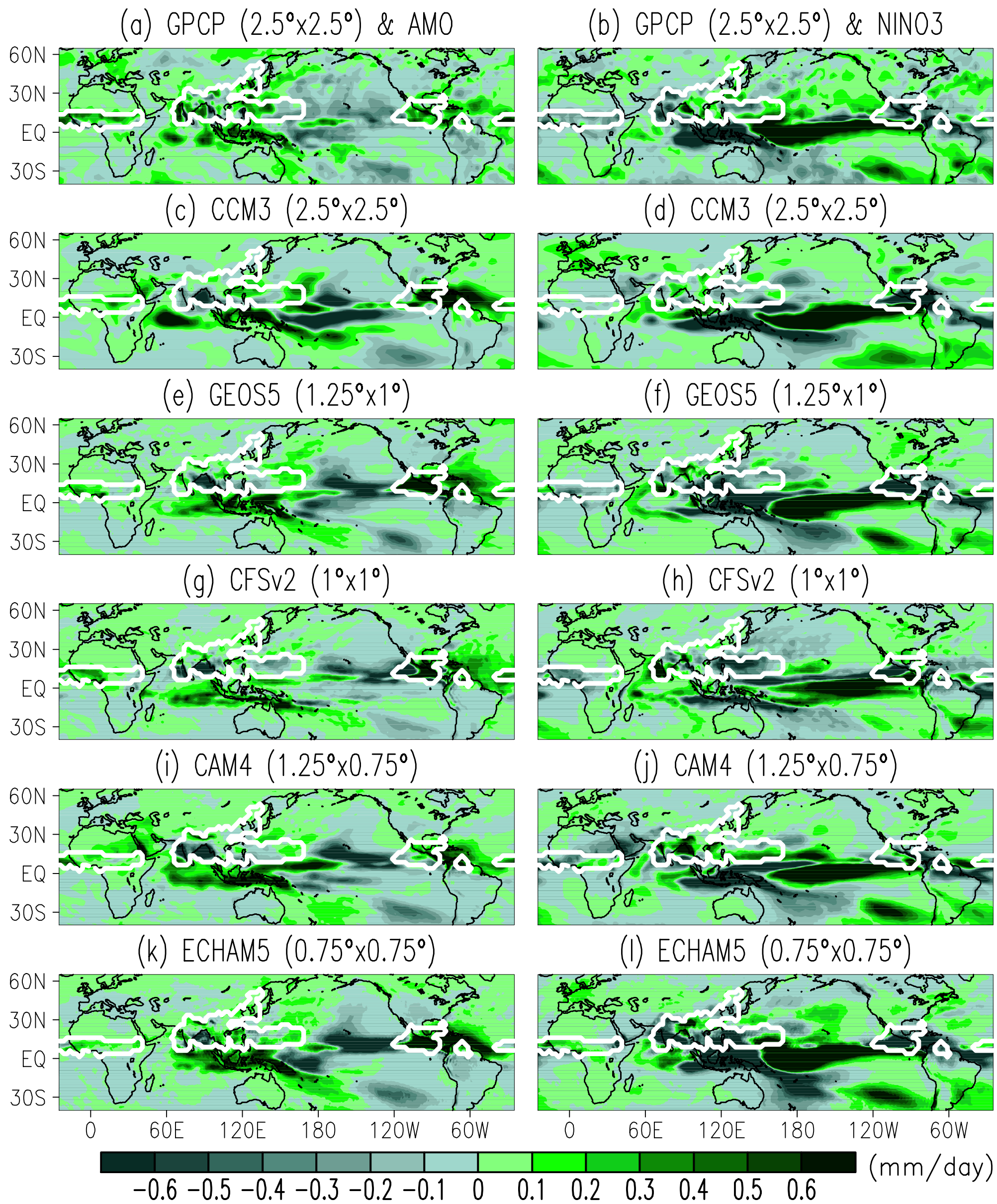

Figure 5. Regression maps of simulated JJAS global precipitation (unit: mm/day) onto the JJAS AMO (left) and NINO3 (right) indices. The AGCMs with different horizontal resolutions are indicated above each subplot.

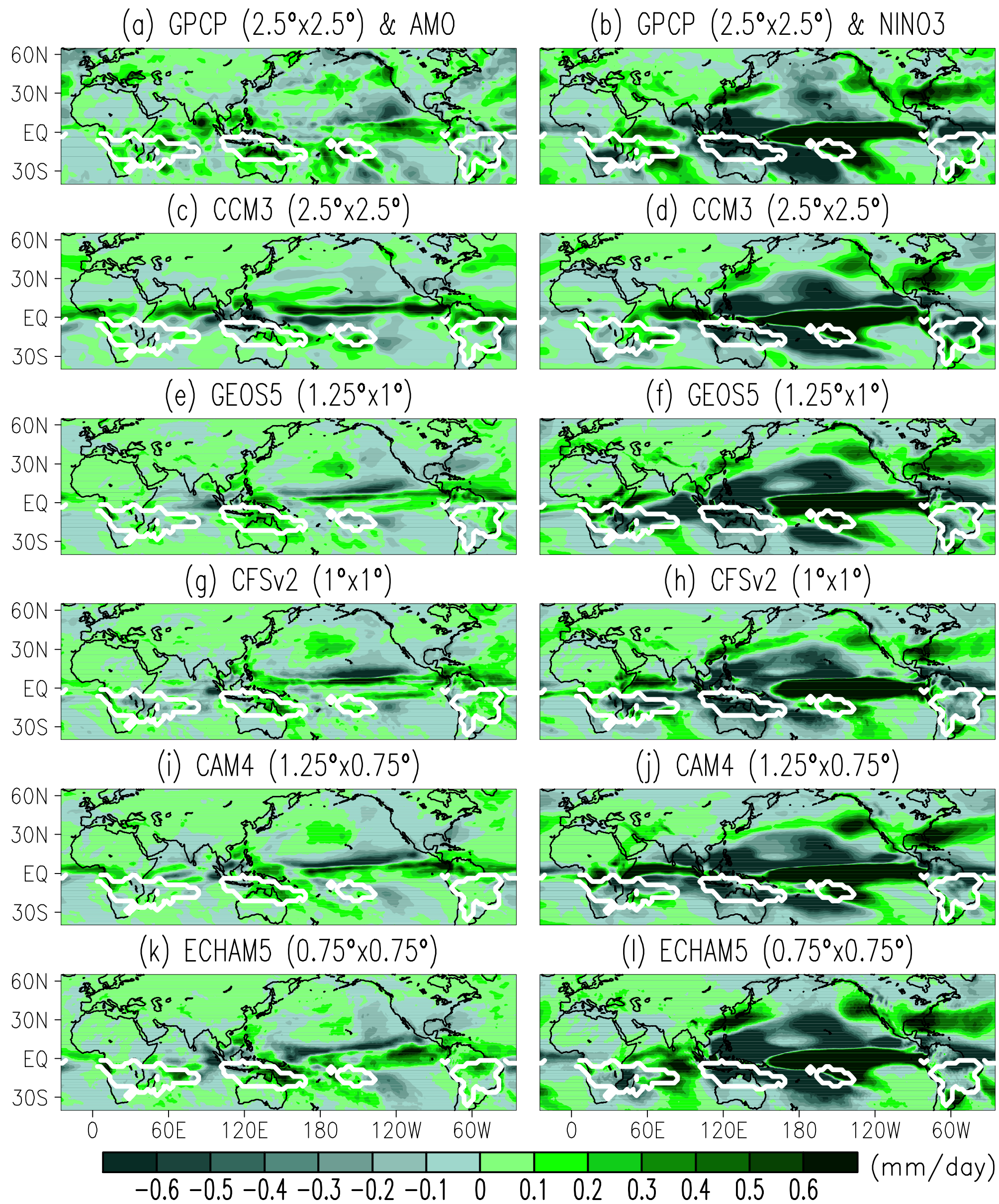

Figure 6. Same as Fig. 5, except for the simulated DJFM global precipitation (unit: mm/day) regressed onto the DJFM AMO (left) and NINO3 (right) indices.

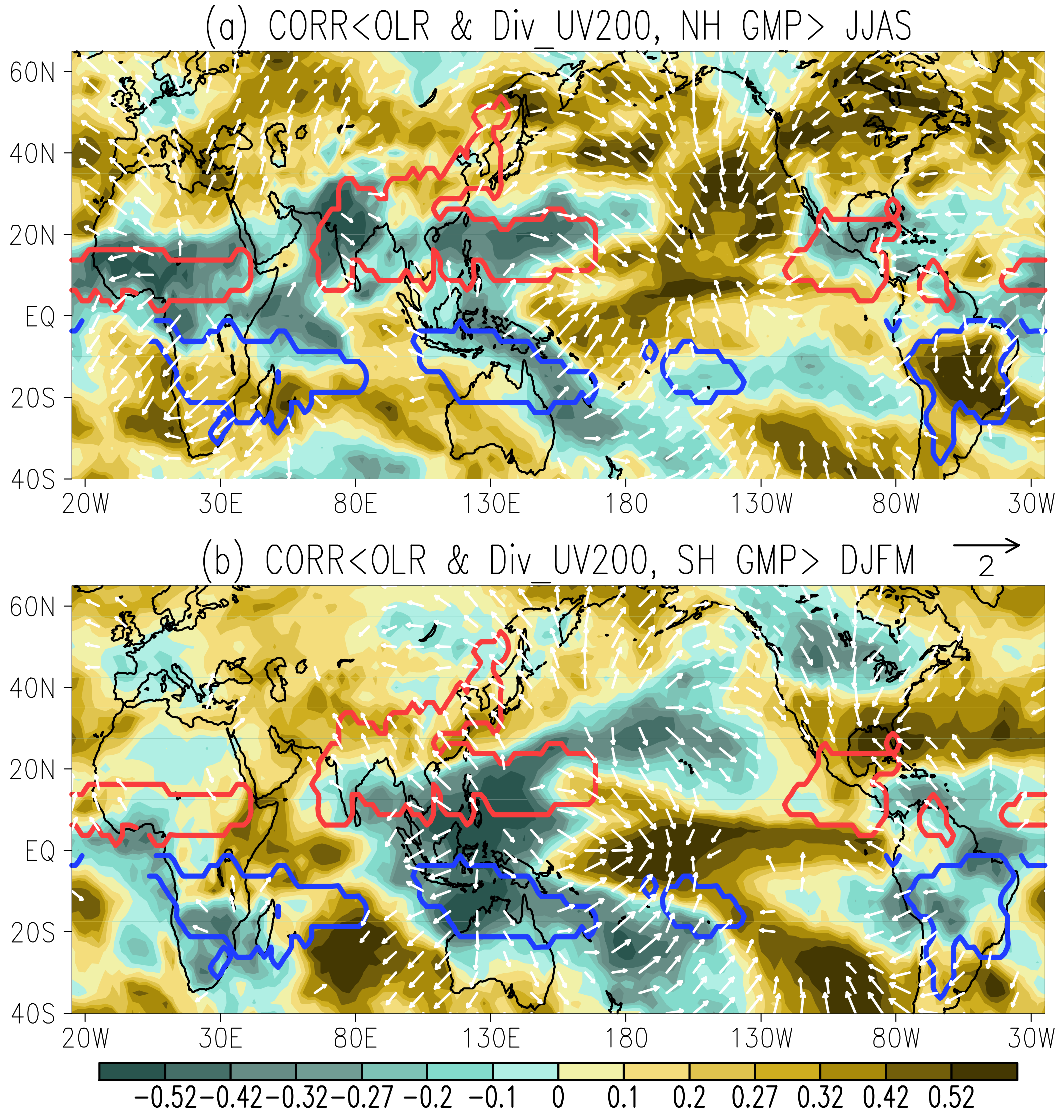

Figure 7. Correlation coefficients of OLR (shading) and 200-hPa divergent wind (vector) with the NH (a) and SH (b) GMP indices obtained from the GPCP data. The magnitudes of vectors indicate the square root of correlation coefficients of zonal and meridional velocities with PCs. The linear trends have been removed from the GMP indices.

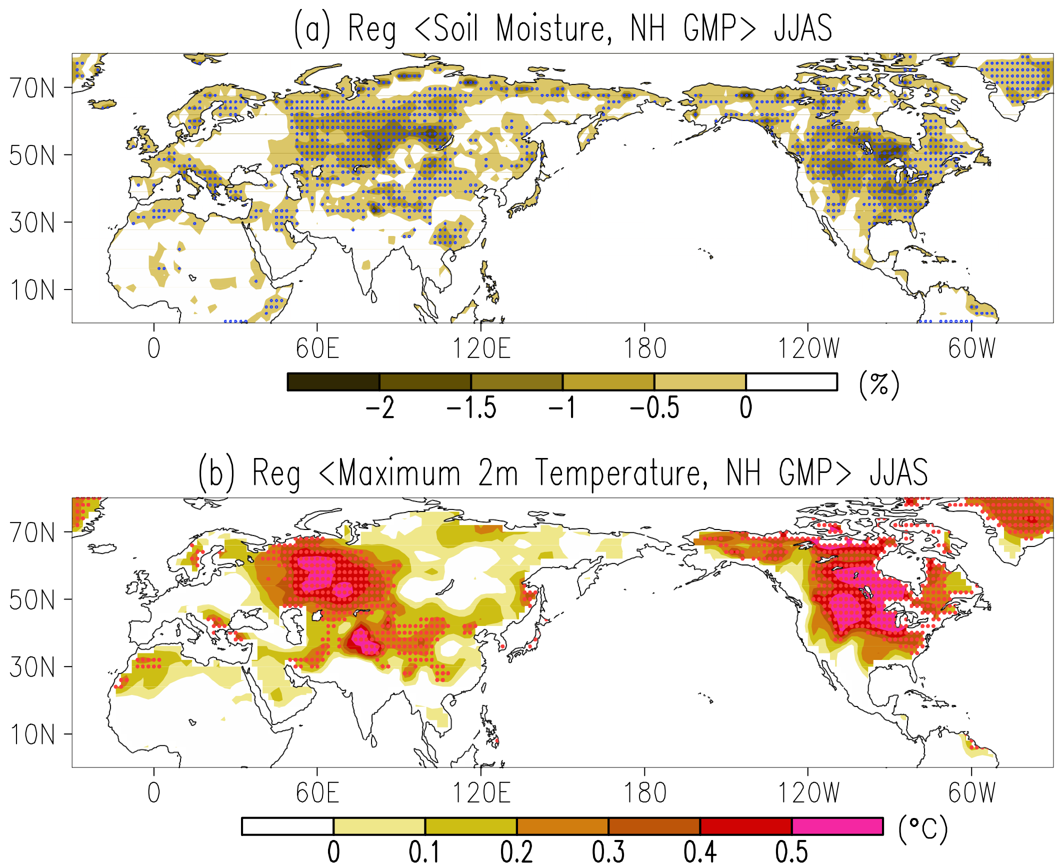

Figure 8. (a) Regression of 0–200 cm soil moisture content (shading) (a) and maximum 2m temperature (Mx2t) (shading) (b) with the GPCP NH GMP index for boreal summer. The dotted areas indicate that the anomalies exceed the 90% confidence levels. The linear trends have been removed from the NH GMP index.

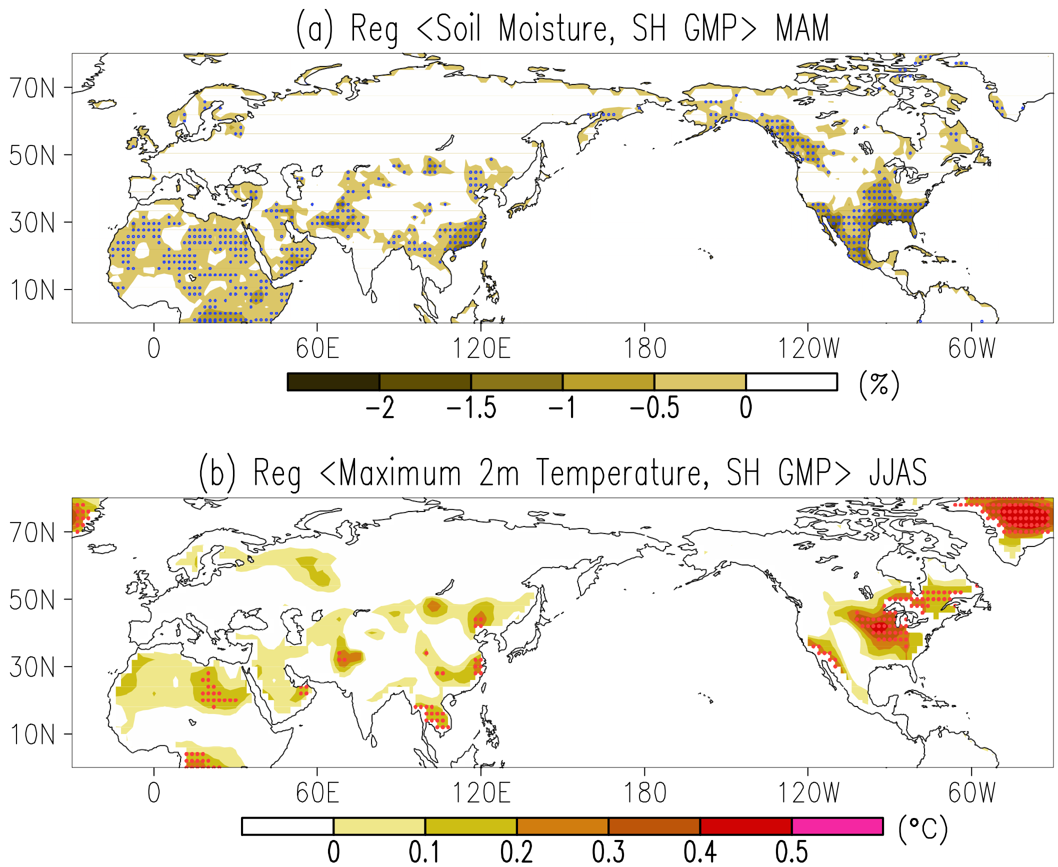

Figure 9. (a) Regression of 0–200 cm soil moisture content (shading) (a) and Mx2t (shading) (b) with the GPCP SH GMP. The soil moisture is for boreal spring, while the Mx2t is for boreal summer (JJAS). The dotted areas indicate that the anomalies exceed the 90% confidence levels. The linear trends have been removed from the SH GMP index.

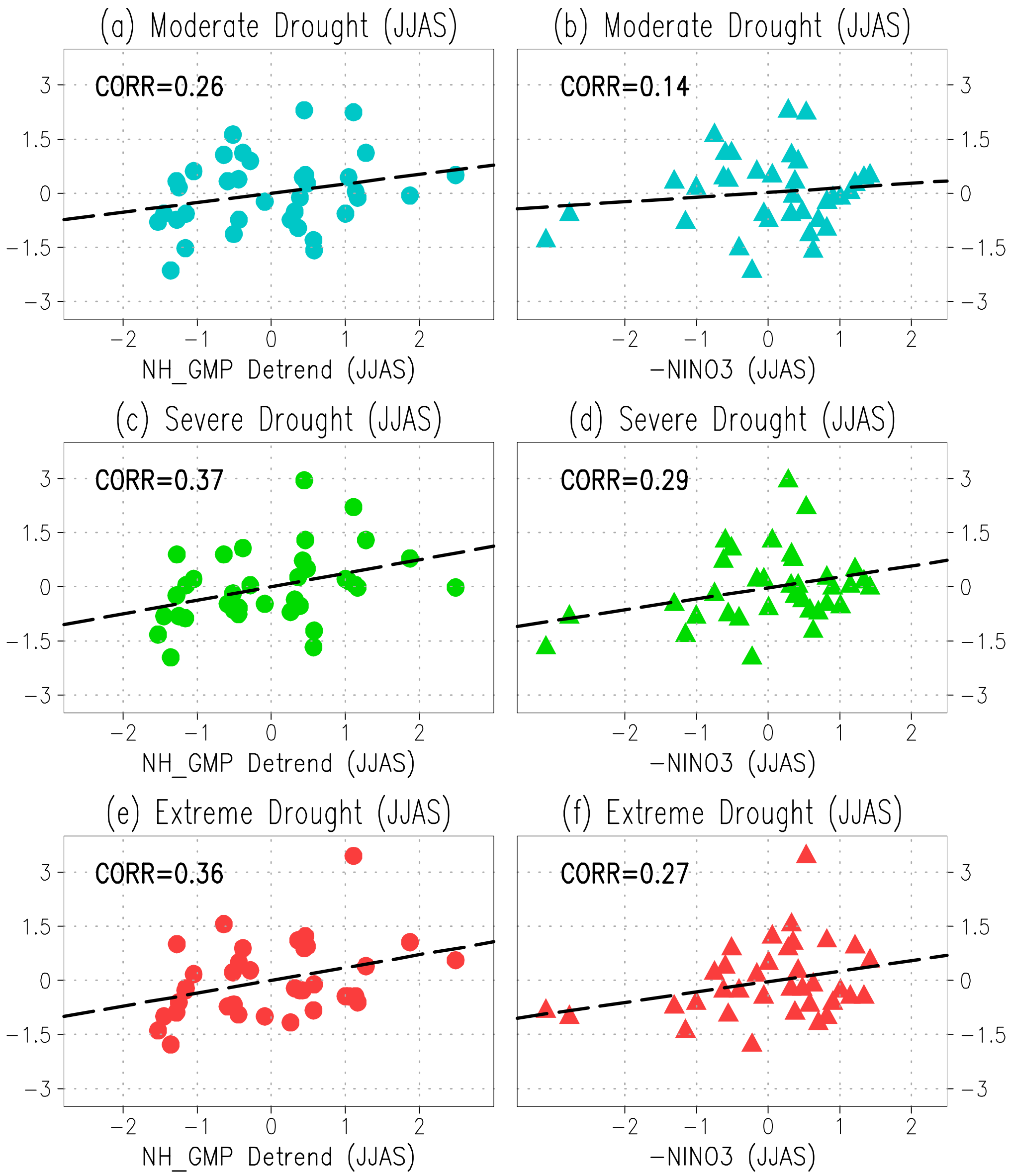

Figure 10. Diagrams of normalized area indices of boreal summer droughts in mid-latitude regions (30°N – 60°N) with respect to the concurrent GPCP NH GMP (left, JJAS)/negative NINO3.4 (right, JJAS), where the linear trends in NH GMP have been removed. The severity of drought is defined in section 2. The calculation of drought area indices are seen in the text. The correlation coefficients (CORR) are plotted in each panel.

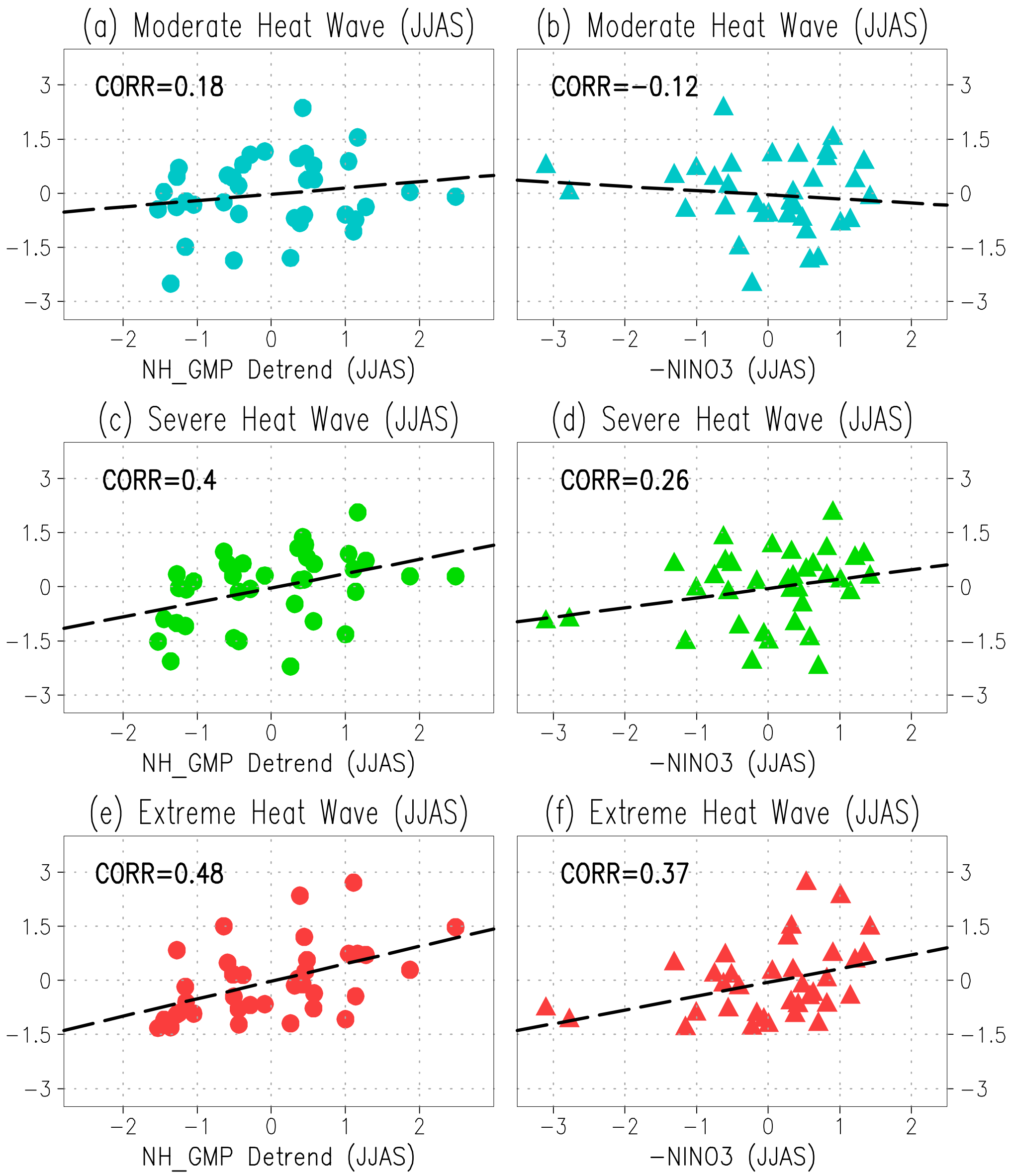

Figure 11. Same as Fig. 10, except for the heat waves (HWs).

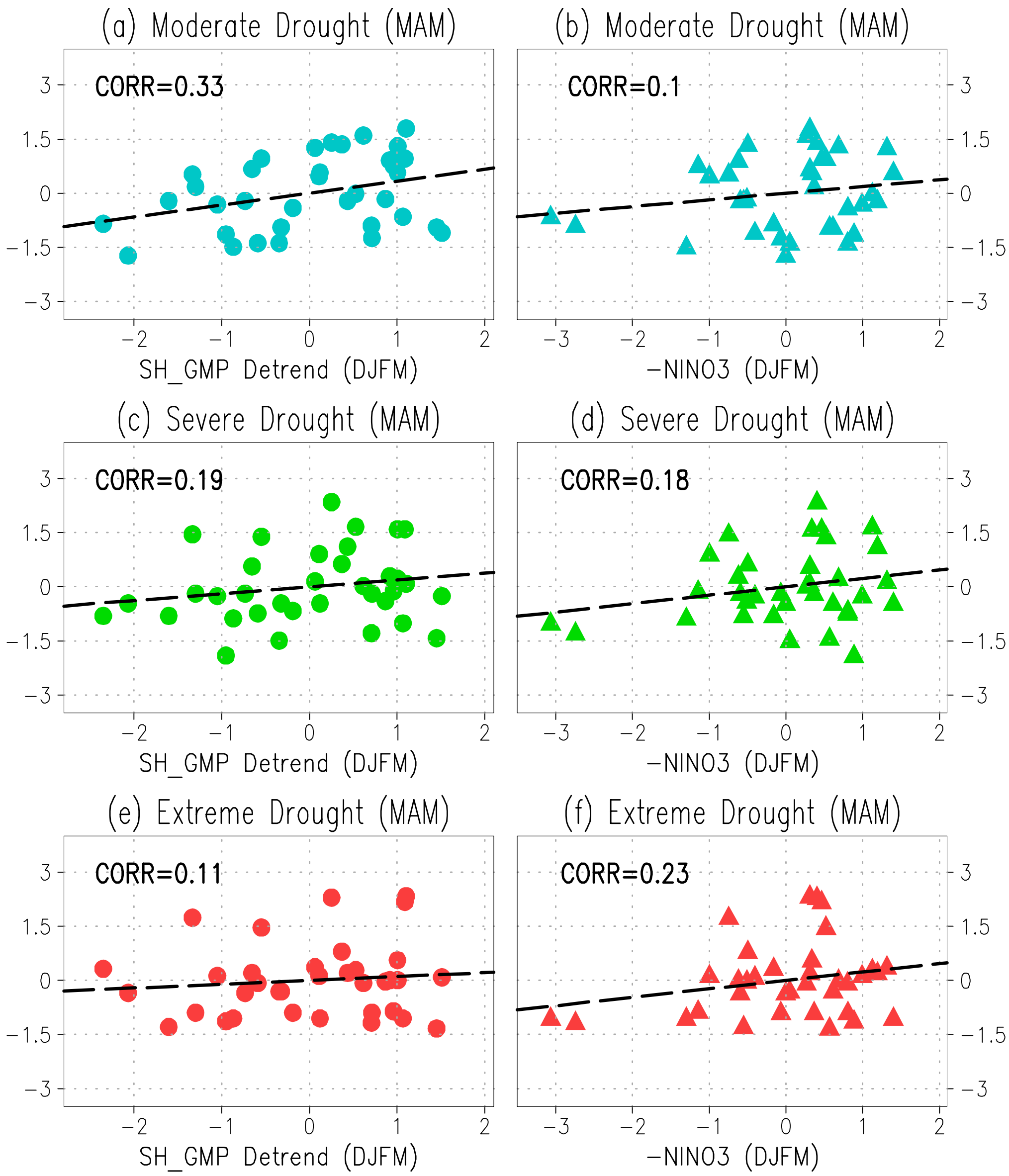

Figure 12. Same as Fig. 10, except for the boreal spring (MAM) droughts in subtropics (10°N – 30°N) with respect to the antecedent GPCP SH GMP (left, DJFM)/negative NINO3 (right, DJFM), where the linear trends in SH GMP have been removed.

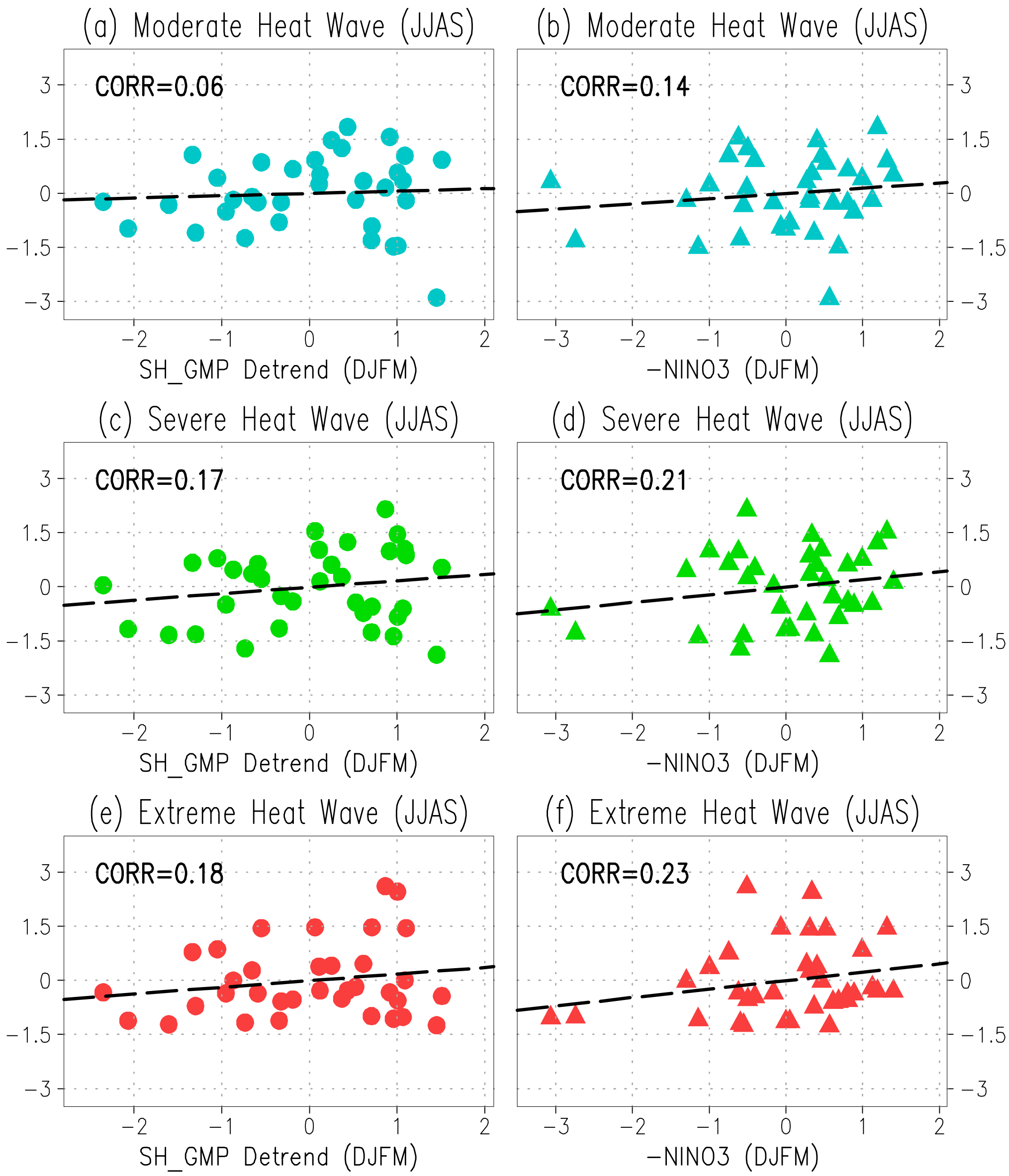

Figure 13. Same as Fig. 10, except for the boreal summer (JJAS) HWs in subtropics (10°N – 30°N) with respect to the antecedent GPCP SH GMP (left, DJFM)/antecedent negative NINO3 (right, DJFM), where the linear trends in SH GMP have been removed.